Nonadiabatic Multielectron Dynamics in Interaction of Molecules with Intense Laser Pulses

by

Andres Felipe Mora

An honors thesis submitted to the

University of Colorado in fulfillment

of the requirements for departmental honors

Bachelor of Science

Department of Physics

2018

This thesis entitled:
Nonadiabatic Multielectron Dynamics in Interaction of Molecules with Intense Laser Pulses
written by Andres Felipe Mora
has been approved for the
Department of Physics

_____
Associate Research Prof. Agnieszka Jaron-Becker

_____
Prof. John Cumulat

_____
Associate Prof. Andreas Becker

_____
Associate Prof. Niels Damrauer

Date _____

The final copy of this thesis has been examined by the signatories, and we find that both the content and the form meet acceptable presentation standards of scholarly work in the above mentioned discipline.

Mora, Andres Felipe (B.S., Engineering Physics)

Nonadiabatic Multielectron Dynamics in Interaction of Molecules with Intense Laser Pulses

Thesis directed by Associate Research Prof. Agnieszka Jaron-Becker

Ultrashort high intensity laser pulses have allowed for the observation of ultrafast dynamics in atoms and molecules. Due to the complexity, these multielectron systems interacting with ultrashort intense laser fields are often theoretically studied using the single active electron approximation (SAE). We present here results of simulations within Time Dependent Density Functional Theory which address the multielectron nature of the studied systems. The results exhibit multielectron effects in form of orbital coupling and nonadiabatic electron dynamics in electron localization, high harmonic generation and ionization of N_2^+ interacting with a strong laser pulse.

Acknowledgements

I would like to thank Agnieszka Jaron-Becker and Andreas Becker for welcoming me into their group and being the best guides through this process and for having patience with me. I would like to also thank all of the graduate students within the group, namely Tennesse, Brynn, Joel, and Cory. Thank you for the help and guidance.

This work utilized the RMACC Summit supercomputer, which is supported by the National Science Foundation (awards ACI-1532235 and ACI-1532236), the University of Colorado Boulder, and Colorado State University. The Summit supercomputer is a joint effort of the University of Colorado Boulder and Colorado State University. [11]

In addition to Summit, the work presented in this thesis utilized the JILA computing clusters for calculations.

Contents

Chapter

Figures

Figure

Chapter 1

Introduction

1.1 Atomic, Molecular and Optical Physics

Research in atomic, molecular and optical (AMO) physics includes many disciplines ranging from the investigation of ultracold quantum gases to the investigation of ultrafast processes occurring in atoms and molecules. Within the realm of ultrafast AMO physics, there exists the strong-field regime which involves the study of the interaction between matter and high intensity fields of the order of 10^{13}-10^{16} W/cm^2. This area of research seeks a means to understand atomic and molecular processes at the fundamental timescales of electron and nuclear dynamics when interacting with intense laser pulses. High intensity lasers have a field strength that is comparable to the Coulomb interaction between the nucleus and electrons. Therefore, the interaction between matter and intense laser pulses can lead to interesting effects such as high harmonic generation.

1.2 High Harmonic Generation

High harmonic generation (HHG) is a highly non-linear process in which visible or infrared (IR) light is converted into light in the soft X-ray and extreme ultraviolet regime [2]. Typically, HHG is observed during the interaction of matter and high intensity fields of the order of 10^{14} W/cm^2. The generated harmonics produced during this interaction appear as integer multiples of the optical driving frequency.

1.2.1 Motivation for HHG

Since the invention of the laser, there have been major challenges to produce coherent radiation at extreme frequencies. High harmonic generation has helped to extend that frequency regime to the X-ray regime. However, the generation of coherent light at extreme frequencies is only one of the many useful properties provided by HHG.

HHG can also be used to image motion at the ultrafast timescale. To understand this, let's consider a fast moving object, such as a horse running. Does the horse at any point have its feet in the air? The human eye cannot process the movement quickly enough to answer to this question. Edward Muybridge developed an experiment in which threads were connected to cameras, which would open and close the "shutter" when the thread was pulled or broken by the horse [12]. This allowed Muybridge to clarify that a horse indeed does have all of its feet in the air at certain points during its gallop. HHG is a process in which light is generated during a period of attoseconds (attosecond = 10^{-18} s). Similarly to the Muybridge's experiment, these pulses may therefore be used as cameras to image electron dynamics occurring at their fundamental timescale of motion in an atom or molecule.

1.2.2 Features of High Harmonic Generation

There are three regimes within an HHG frequency spectrum as shown in Figure 1.1.

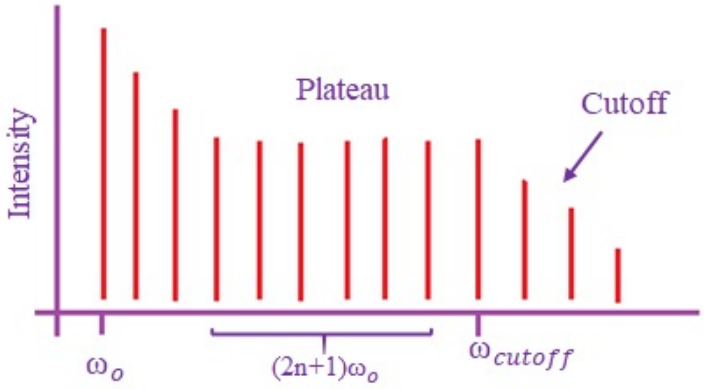

Figure 1.1: Schematic HHG spectrum due to interaction of atom or molecule with a linearly polarized electric field. The first regime is the perturbative regime in which the harmonic's strength decreases exponentially. The second regime is the non-perturbative regime where harmonics of similar intensity are observed. Beyond a cutoff frequency the harmonics decrease rapidly.

The first part is the perturbative regime which occurs at low harmonic frequencies, typically up to the 3^{rd}-5^{th} harmonic. The regime that follows is a plateau in which higher order harmonics of similar intensities are generated. At the end of this plateau there is a cutoff beyond which the generated harmonics are greatly reduced in intensity. The cutoff frequency can be determined using the following semi-classical formula,

$$\hbar\omega_{cutoff} = |I_p| + 3.17U_p, \tag{1.1}$$

where I_p is the ionization energy of the electron, and U_p is the ponderomotive energy which is the cycle-averaged energy of an electron interacting with a laser field, given by

$$U_p = \frac{e^2 E_o^2}{4m\omega^2}, \tag{1.2}$$

where e is the charge of the electron, E_o is the amplitude of laser, m is the electron mass, and ω is the frequency of the laser. For systems that have inversion symmetry such as atoms and molecules, only odd harmonics are observed in their respective HHG spectra.

Occurrence of this regime is a typical sign of the non-perturbative interaction between the

laser field and the electrons of the atom or molecule.

1.2.3 Semi-Classical Picture of High-Harmonic Generation

High Harmonic generation can be described in a simplified way using a semi-classical picture as given by the so-called three-step model shown in Figure 1.2.

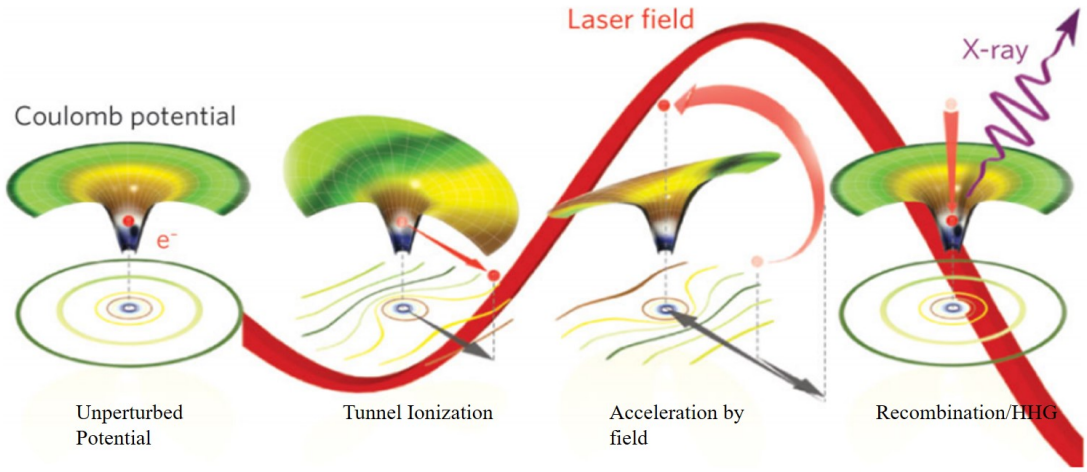

Figure 1.2: Three-step semi-classical model of high harmonic generation [2].

The three-step model states that atoms or molecules subjected to a high intensity infrared pulse absorb multiple photons, and an electron is set free. The electron is first accelerated away from the potential but when the field of the pulse reverses direction, the electron is accelerated back towards the nucleus, and recombines into its initial bound state. During the recombination a high harmonic photon is emitted.

1.3 High Harmonic Generation from Molecules

Typically, atoms interacting with a linearly polarized laser emit linearly polarized high harmonics. However, it has been found that the generation of high harmonics from molecules interacting with a linearly polarized laser is much more complex and interesting. For example, elliptically polarized harmonics can be generated. This occurs due to the non spherical

symmetry of the molecular orbitals.

In test calculations we have determined the ellipticity of harmonics from H_2^+. To this end we have performed various simulations (for details of theory and simulations, see next section) for H_2^+ interacting with an 800 nm laser field at an intensity I = 3×10^{14} W/cm^2, where the orientation angle of the molecular axis with respect to the polarization direction of the laser field was rotated in increments within the interval [0,π/2]. For linear molecules such as H_2^+, there is a parallel and perpendicular dipole acceleration component. A Fourier transform of the dipole components is taken and then we determine the ellipticity of the harmonics as:

$$\epsilon = \sqrt{\frac{1 + r^2 - \sqrt{1 + 2r^2 cos(2\delta) + r^4}}{1 + r^2 + \sqrt{1 + 2r^2 cos(2\delta) + r^4}}} \tag{1.3}$$

where r is the amplitude ratio between the perpendicular and parallel components given by

$$r = \frac{|d_\perp(\omega)|}{|d_\parallel(\omega)|}, \tag{1.4}$$

and δ is the phase difference between both components:

$$\delta = arg[d_\perp(\omega)] - arg[d_\parallel(\omega)] \tag{1.5}$$

Our results (see Figure 1.3) indeed show that high harmonics from H_2^+ are elliptically polarized; ellipticity of the odd harmonics is shown for the following orientations of the molecular axis with respect to the field, namely: 0°, 30°, 45°, 60°, and 90°.

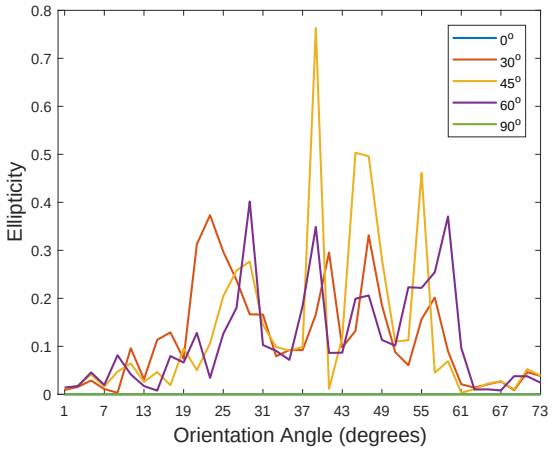

(a)

Figure 1.3: Plot of ellipticity vs. harmonics of H_2^+ for various angles of the molecular axis with respect to the polarization direction of the laser field.

It is evident that the harmonics produced exhibit the largest ellipticity when the molecule is oriented at 45° with respect to the laser field. Further analysis indicates that the 39^{th} harmonic exhibits the largest ellipticity. At this angle, the parallel and perpendicular dipole components are close in magnitude, thus r being 1, and the phase difference between them being $\pi/2$. Figure 1.4 shows the results for the amplitude ratio and phase difference of the 39^{th} harmonic as well as a few nearby harmonics for various orientations.

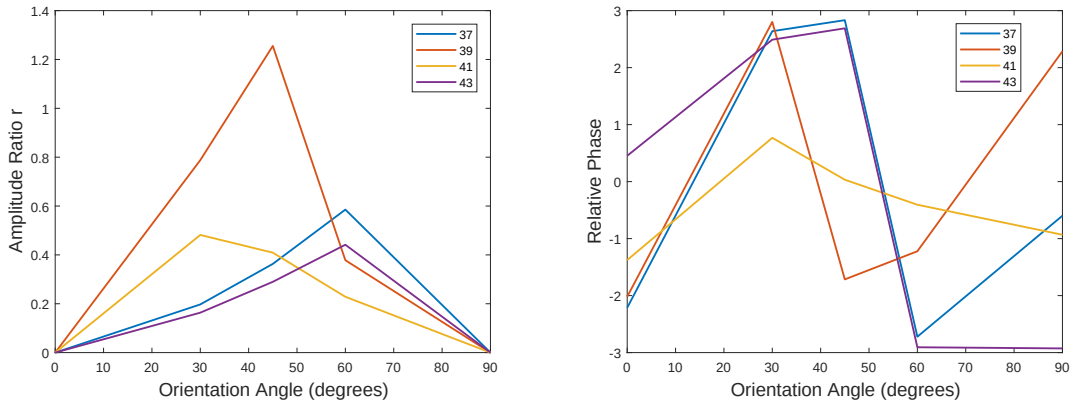

(a) (b)

Figure 1.4: (a) Amplitude ratio r and (b) relative phase δ as a function of orientation angle for the 37^{th}, 39^{th}, 41^{st}, and 43^{rd} harmonics.

Therefore, our theoretical results show that largest ellipticity is achieved at an orientation angle of 45°. This is close to the results obtained by Chu et al. [10], which suggest that the maximum ellipticity occurs at a 50° orientation.

Chapter 2

Time-Dependent Density-Functional Theory

2.1 Multielectron Systems

Atoms and molecules are multielectron systems. A system of N electrons interacting with a laser field can be described by its wavefunction $\Psi(t, \mathbf{r})$ ($\mathbf{r} = [\mathbf{r}_1,...,\mathbf{r}_N]$) which obeys the time-dependent Schrödinger equation:

$$H(\mathbf{r}, t)\Psi(\mathbf{r}, t) = i\frac{\partial\Psi(\mathbf{r}, t)}{\partial t}, \tag{2.1}$$

where the Hamiltonian H is written in the form

$$H(\mathbf{r}, t) = T(\mathbf{r}) + V_{ee}(\mathbf{r}) + V_{ne}(\mathbf{r}) + V_{laser}(\mathbf{r}, t), \tag{2.2}$$

with $T(\mathbf{r})$ being the kinetic energy of the electrons

$$T(\mathbf{r}) = -\frac{1}{2}\sum_{i=1}^{N}\nabla_i^2. \tag{2.3}$$

The second term denoted $V_{ee}(\mathbf{r})$ is the electron-electron interaction which has the form

$$V_{ee}(\mathbf{r}) = \sum_{i<j=1}^{N}\frac{1}{|\mathbf{r}_i - \mathbf{r}_j|}, \tag{2.4}$$

$V_{ne}(\mathbf{r})$ corresponds to the nuclear-electron interaction given by

$$V_{ne}(\mathbf{r}) = \sum_{i,k} \frac{Z_k}{|\mathbf{r}_i - \mathbf{R}_k|}, \tag{2.5}$$

where $\mathbf{R}_k$ is the position and Z_k is the charge of the k^{th} nucleus. The last term $V_{laser}(\mathbf{r}, t)$ includes the interaction between the electrons and the applied laser field

$$V_{laser}(\mathbf{r}, t) = E_o f(t) sin(\omega t) \sum_{i=1}^{N} \mathbf{r}_i \cdot \hat{n}, \tag{2.6}$$

where E_o is the amplitude of the electric field, $f(t)$ is the envelope of the pulse, ω is the frequency of the laser, and $\hat{n}$ is the polarization direction of the field.

While the multielectron Schrödinger equation describes the system fully, it is computationally expensive to solve for $\Psi(\mathbf{r}, t)$ in the case of larger systems. Due to this, it is indeed currently impossible to exactly solve the multielectron Schrödinger equation for systems with more than two electrons interacting with intense laser pulses in a reasonable amount of time. Fortunately, there exists an alternative approach to approximately solve multielectron systems known as Density Functional Theory (DFT).

2.2 Density Functional Theory

The basis of DFT comes from the Hohenberg-Kohn (HK) theorems [6,7] which state that the external potential $V_{ext}(\mathbf{r})$ of the system is a functional of the electron density $\rho(\mathbf{r})$, and that the ground state of a system can be determined by its electronic density given by

$$\rho_{gs}(\mathbf{r}) = N \int d\mathbf{r}_N \Psi^*_{gs}(\mathbf{r}) \Psi_{gs}(\mathbf{r}). \tag{2.7}$$

In other words, the ground state wavefunction $\Psi_{gs}(\mathbf{r})$ is a functional of the ground state

density $\rho_{gs}(\mathbf{r})$, so it can be written as

$$\Psi_{gs}(\mathbf{r}) = \Psi_{gs}[\rho_{gs}(\mathbf{r})]. \tag{2.8}$$

This then leads to the fact that any observable corresponding to the ground state is also a functional of the density $\rho_{gs}(\mathbf{r})$

$$O[\rho_{gs}(\mathbf{r})] = \langle \Psi_{gs}[\rho_{gs}(\mathbf{r})]|O|\Psi_{gs}[\rho_{gs}(\mathbf{r})]\rangle. \tag{2.9}$$

Therefore the energy of the system is also a functional of the density $\rho_{gs}(\mathbf{r})$.

2.3 Kohn-Sham Equations

Since it has been established that the observables of a system are functionals of the density $\rho_{gs}(\mathbf{r})$, we need to consider ways to solve for the density. This can be done using the Kohn-Sham equations.

Consider a system of noninteracting particles in an arbitrary external potential V_s of the form

$$V_s(\mathbf{r}) = \int d\mathbf{r}\rho(\mathbf{r})v_s(\mathbf{r}), \tag{2.10}$$

where the Hamiltonian is given by

$$H_s = T + V_s. \tag{2.11}$$

The first term in the Hamiltonian is the kinetic energy of the electron given by

$$T = -\frac{1}{2}\sum_{i=1}^{N} \nabla_i^2. \tag{2.12}$$

Since the particles are non-interacting, a Slater determinant can be used to approximate the

ground state wavefunction $\Psi_{gs}(\mathbf{r})$ of the N-particle system:

$$\Psi_{gs}(\mathbf{r}) = \frac{1}{\sqrt{N!}} \begin{vmatrix} \phi_1(\mathbf{r}_1) & \phi_1(\mathbf{r}_2) & \phi_1(\mathbf{r}_3) & \dots & \phi_1(\mathbf{r}_N) \\ \phi_2(\mathbf{r}_1) & \phi_2(\mathbf{r}_2) & \phi_2(\mathbf{r}_3) & \dots & \phi_2(\mathbf{r}_N) \\ \vdots & \vdots & \vdots & & \vdots \\ \phi_N(\mathbf{r}_1) & \phi_N(\mathbf{r}_2) & \phi_N(\mathbf{r}_3) & \dots & \phi_N(\mathbf{r}_N) \end{vmatrix} \tag{2.13}$$

where the orbitals $\phi_i(\mathbf{r})$ are solutions to the single particle Schrödinger equation

$$-\frac{1}{2}\nabla^2\phi_i(\mathbf{r}_i) + V_s(\mathbf{r}_i)\phi_i(\mathbf{r}_i) = \epsilon_i\phi_i(\mathbf{r})_i, \tag{2.14}$$

and the ground state density of the N electron system is given by

$$\rho_{gs}(\mathbf{r}) = \sum_{i=1}^{N} |\phi_i(\mathbf{r})|^2. \tag{2.15}$$

In this case the HK theorem applies and there exists a one to one mapping between the ground state density $\rho(\mathbf{r})$ and the potential $V_s(\mathbf{r})$. The energy of the system is given by

$$E_{s,gs}[\rho] = T_s[\rho_{gs}] + \int d\mathbf{r}\rho(\mathbf{r})v_s(\mathbf{r}) = \sum_{i=1}^{N} \int d\mathbf{r}\phi_i^*(\mathbf{r})(-\frac{1}{2}\nabla_i^2)\phi_i(\mathbf{r}) + \int d\mathbf{r}\rho(\mathbf{r})v_s(\mathbf{r}). \tag{2.16}$$

Now consider a system of interacting particles with an external potential denoted by $V_{ext}(\mathbf{r})$. The ground state density $\rho_{gs}(\mathbf{r})$ for this system can be obtained from the ground state density of a system of noninteracting particles with a potential denoted by $V_s(\mathbf{r})$. This turns the problem of solving a multielectron Schrödinger equation into multiple noninteracting single particle Schrödinger-like equations. In turn, this greatly reduces the computational costs needed to numerically solve such systems.

For a system of interacting particles the energy functional is given by

$$E[\rho_{gs}] = T_s[\rho_{gs}] + V_H[\rho_{gs}] + E_{xc}[\rho_{gs}] + V[\rho_{gs}]. \tag{2.17}$$

The second term $V_H[\rho_{gs}]$ is the Hartree energy (classical Coulomb energy) which is given by

$$V_H[\rho_{gs}] = \frac{1}{2}\int d\mathbf{r}\int d\mathbf{r}'\frac{\rho_{gs}(\mathbf{r})\rho_{gs}(\mathbf{r}')}{|\mathbf{r}-\mathbf{r}'|}, \tag{2.18}$$

while $E_{xc}[\rho_{gs}]$ is the exchange correlation energy:

$$E_{xc}[\rho_{gs}] = T[\rho_{gs}] - T_s[\rho_{gs}] + U[\rho_{gs}] - \frac{1}{2}\int d\mathbf{r}\int d\mathbf{r}'\frac{\rho_{gs}(\mathbf{r})\rho_{gs}(\mathbf{r}')}{|\mathbf{r}-\mathbf{r}'|}. \tag{2.19}$$

Taking the derivative of the exchange correlation energy, gives the exchange correlation potential

$$V_{xc}[\rho_{gs}] = \frac{\delta E_{xc}}{\delta \rho_{gs}}. \tag{2.20}$$

This potential has an unknown form, but can be approximated for different systems.

For a system of interacting particles the variational principle with respect to the electron density results in

$$0 = \frac{\delta T_s[\rho_{gs}]}{\delta \rho_{gs}} + \frac{\delta V[\rho_{gs}]}{\delta \rho_{gs}} + \frac{\delta V_H[\rho_{gs}]}{\delta \rho_{gs}} + \frac{\delta E_{xc}[\rho_{gs}]}{\delta \rho_{gs}} \tag{2.21}$$

Similarly, for a system of noninteracting particles the variational principle with respect to density yields

$$\frac{\delta E_{xc}[\rho_{gs}]}{\delta \rho_{gs}} = 0 = \frac{\delta T_s[\rho_{gs}]}{\delta \rho_{gs}} + \frac{\delta V_s[\rho_{gs}]}{\delta \rho_{gs}} \tag{2.22}$$

Comparing the variational principle for both the interacting and noninteracting system, we get

$$v_s(\mathbf{r}) = v_{ext}(\mathbf{r}) + v_H(\mathbf{r}) + v_{xc}(\mathbf{r}), \tag{2.23}$$

to achieve both minimizations resulting in the same electron density $\rho_s(\mathbf{r}) = \rho(\mathbf{r})$. This implies that the density of an interacting system within an external potential $v_{ext}(\mathbf{r})$ can be determined by solving the Schrödinger equation for many non-interacting particles within a potential $v_s(\mathbf{r})$, only if the exchange-correlation potential is known. Based on this assumption, the orbitals of the noninteracting system can be obtained by solving the Kohn-Sham (KS) equation, given by

$$-\frac{1}{2}\nabla^2\phi_i(\mathbf{r}) + v_s(\mathbf{r})\phi_i(\mathbf{r}) = \epsilon_i\phi_i(\mathbf{r}), \tag{2.24}$$

and the electron density of the interacting system can then be obtained via

$$\rho(\mathbf{r}) = \sum_{i=1}^{N} f_i|\phi_i(\mathbf{r})|^2, \tag{2.25}$$

where the term f_i is the electron population in a given orbital i.

The KS equations must be solved self-consistently because both the terms $v_H(\mathbf{r})$ and $v_{xc}(\mathbf{r})$ depend on the density $\rho(\mathbf{r})$, which depends on the orbitals $\phi_i(\mathbf{r})$, which in turn depends on $v_s(\mathbf{r})$. Due to this, the calculation starts with an initial guess for the electron density $\rho(\mathbf{r})$, then the potential $v_s(\mathbf{r})$ is obtained, which leads to a solution of the KS equation $\phi_i(\mathbf{r})$, which then yields a new density $\rho(\mathbf{r})$. This process is repeated until the system converges to the correct ground state density. Once convergence is obtained, then observables for the system can be calculated.

2.4 Runge-Gross Theorem

The Runge-Gross theorem [6,7] states that given two electron densities $n(\mathbf{r}, t)$ and $n'(\mathbf{r}, t)$, both obtained from an initial wave function Ψ_o which is influenced by two different potentials $v(\mathbf{r}, t)$ and $v'(\mathbf{r}, t)$, will become infinitely different after a given time. This implies that there is a one-to-one mapping between densities and potentials obtained from a given

initial wavefunction.

$$\rho(\mathbf{r},t) \rightarrow V(\mathbf{r},t) \rightarrow \Psi(\mathbf{r},t) \tag{2.26}$$

2.5 Time-Dependent Density Functional Theory (TDDFT)

An extension of DFT beyond the static potential is TDDFT, which considers the system being subjected to a time dependent external potential, typically from an induced field which is of the form of equation (2.6).

There are several assumptions made in this description

(1) The field is treated classically since at high intensities the field has a large photon density.

(2) The dipole approximation is used, which holds when the wavelength of the laser field is larger than the size of the system.

The field is treated as purely electric, and its magnetic component can be neglected.

In the case of a time dependent external potential, the Runge-Gross theorem states that there is a one-to-one mapping between the electron density $\rho(\mathbf{r},t)$ and the external potential $v(\mathbf{r},t)$. Therefore, instead of solving a many body time dependent Schrödinger equation, the density can be found by using the time dependent Kohn-Sham equation given by

$$-\frac{1}{2}\nabla^2\phi_i(\mathbf{r},t) + v_{ks}(\mathbf{r},t)\phi_i(\mathbf{r},t) = i\frac{\partial}{\partial t}\phi_i(\mathbf{r},t), \tag{2.27}$$

where for the time-dependent case, the external potential includes the potential from the laser field. By solving the time-dependent Kohn-Sham equations the time-dependent density is then given by

$$\rho(\mathbf{r},t) = \sum_{i=1}^{N} f_i|\phi_i(\mathbf{r},t)|^2, \tag{2.28}$$

where $\phi_i(\mathbf{r},t)$ is the i^{th} time-dependent Kohn-Sham orbital and f_i is the occupation number.

2.6 Implementation of TDDFT

The solution of the KS equation can be found numerically by discretizing both the time and spatial components. This converts the KS equation into a matrix equation. To obtain the initial wavefunction, the eigenvalue problem is solved self-consistently with an initial guess for the ground state needed. After the ground state of the system has been obtained, the wavefunction can be propagated in time. There are a variety of methods available to numerically solve the KS equations [9].

Given some initial wavefunction for the i^{th} orbital $\psi(t=0)$, time evolution states that after some time Δt the wavefunction is

$$\psi_j(t+\Delta t) \approx \frac{1 - i\frac{\Delta t}{2}H(t+\frac{\Delta t}{2})}{1 + i\frac{\Delta t}{2}H(t+\frac{\Delta t}{2})}\psi(t). \tag{2.29}$$

The Hamiltonian operator $H(t)$ can be evaluated by using a finite difference scheme [9] where the wavefunction of the system is defined on a discrete spatial and temporal grid.

For the results presented in this thesis, all of the simulations were performed using the ab-initio TDDFT software Octopus [3,4,5]. The simulations for N_2^+ were performed at its equilibrium bond length with a trapezoidal pulse shape at a wavelength of 400 nm, 600 nm, and 800 nm. In addition, the simulation grid used is spherically shaped with a varying radius depending on intensity of the pulse. The exchange correlational functional used in the simulations was the local-density approximation (LDA) for a spin-polarized system [13] and an average-density self-interaction correction was used [14].

Chapter 3

Electron Localization

Indication for the occurrence of multielectron effects can be seen from the behavior of the electrons inside the molecule, when driven by the oscillating field of the laser. Electron localization therefore provides a means to study the response of the electrons to the field, and gives an insight of the electron dynamics occurring in molecules. To visualize electron localization, the density $\rho(\mathbf{r}, t)$ obtained by solving the Kohm-Sham equations is integrated over two spatial dimensions not including the dimension of the molecular axis.

$$\rho(z, t) = \int \rho(\mathbf{r}, t) dx dy \tag{3.1}$$

The ground state density $\rho(z, t = 0)$ is then subtracted from $\rho(z, t)$ and the resulting density difference is then plotted.

$$\Delta\rho(z, t) = \rho(z, t) - \rho(z, t = 0) \tag{3.2}$$

3.1 Molecular Orbital Diagram and Properties of N_2^+

Open shell molecules such as N_2^+ in their ground state equilibrium geometries have a higher ionization potential than their neutral counterparts, which in turn extends the plateau cutoff for HHG [15,16]. Figure 3.1 shows the molecular orbital diagram of N_2^+ as well as the energies of each orbital.

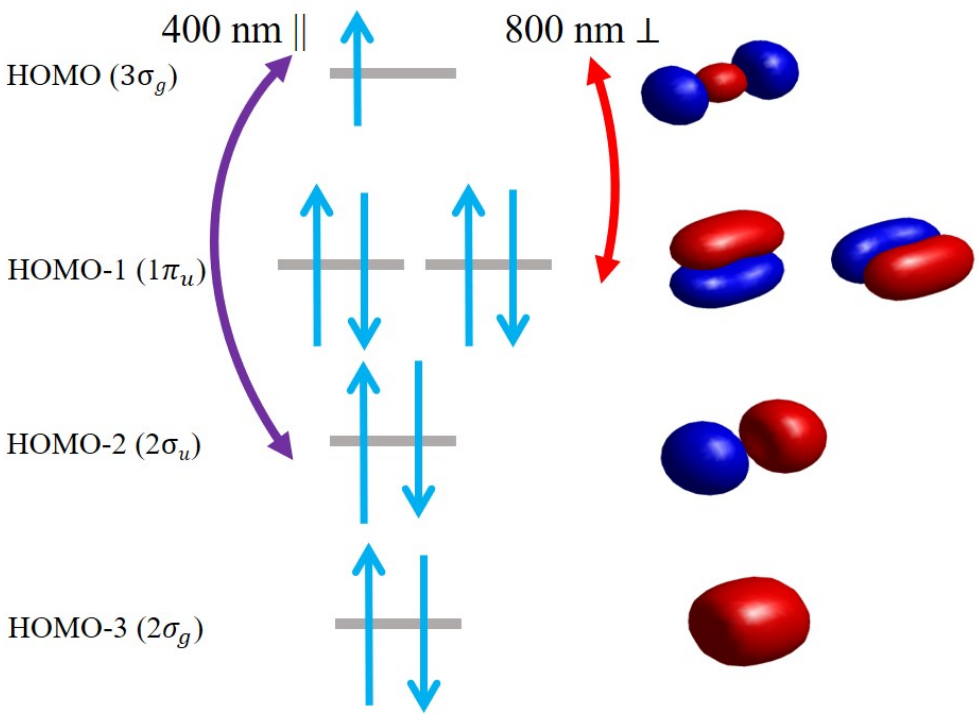

Figure 3.1: N_2^+ molecular orbital diagram and energies.

As shown above, the HOMO and HOMO-1 have a energy difference that corresponds to a wavelength of 800 nm, while the HOMO and HOMO-2 have an energy difference corresponding to 400 nm. In the presence of a laser field whose optical frequency is tuned to the frequency corresponding between energy difference of the orbitals, then a resonant coupling can be induced, which then induces multielectron effects, as we will show in this thesis.

3.2 Non-Adiabatic Electron Dynamics

When the applied laser field induces a resonant coupling between orbitals a non-adiabatic behavior of the electron density becomes present. For N_2^+ this resonant coupling occurs e.g when the laser field has a wavelength of 400 nm and its polarization direction is oriented along the molecular axis. Figure 3.2 shows the electron localization along the molecular axis of N_2^+ interacting with lasers of different wavelengths as a function of time.

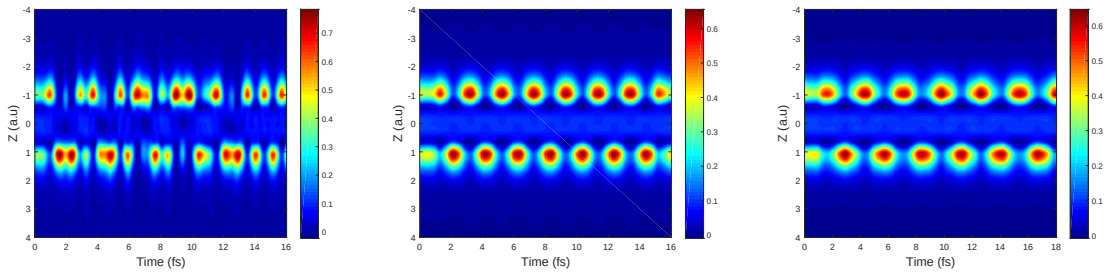

(a) (b) (c)

Figure 3.2: Visualization of electron localization of N_2^+ along the molecular axis at different laser wavelengths as a function of time: (a) 400 nm laser field of intensity I = 2×10^{14} W/cm^2, (b) 600 nm laser field of intensity I = 2×10^{14} W/cm^2 , and (c) 800 nm laser field of intensity I =2×10^{14} W/cm^2. In all cases the orientation of the polarization is parallel to the molecular axis.

As can be seen electron localization exhibits a strong non-adiabatic behavior when the laser is at the resonant wavelength of 400 nm. As the wavelength is increased and the field becomes more non-resonant, the non-adiabatic behavior diminishes and the behavior is adiabatic, i.e the electron follows the oscillation of the electric field. When the laser wavelength is equal to 600 nm, which is near resonant, there is some non-adiabatic behavior still present as can be seen by the non-symmetric oscillations of the electron density projection difference. At the non-resonant case of 800 nm, the behavior is almost fully adiabatic. The visualization of the electron localization shows that non-adiabatic behavior in the electron dynamics is brought upon by the laser induced coupling of the HOMO and HOMO-2 states in N_2^+ when interacting with a 400 nm laser field, as long as the polarization direction is parallel to the molecular axis.

3.3 Dependence of Non-Adiabatic Behavior on Intensity

Non-adiabatic behavior is here observed within the strong-field regime. It is therefore useful to visualize electron localization at different laser intensities and see how the dynamics vary. Several simulations of N_2^+ interacting with a 400 nm laser oriented parallel to the molecular axis were performed at the following intensities: 1×10^{13} W/cm^2, 5×10^{13} W/cm^2,

2×10^{14} W/cm^2, and 5×10^{14} W/cm^2. The results for electron localization are shown in Figure 3.3.

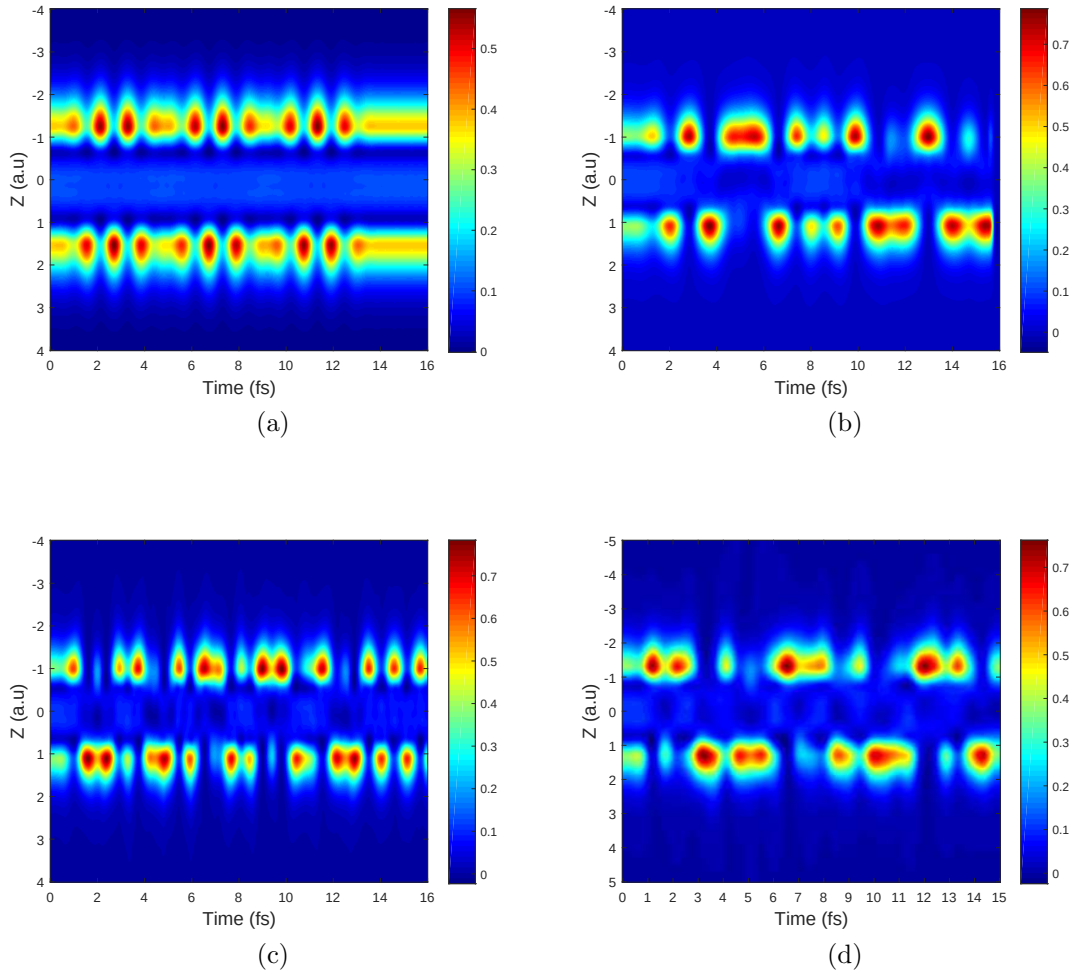

Figure 3.3: Visualization of rising non-adiabatic behavior within the electron localization of N_2^+ under the influence of a 400 nm laser at intensities (a) 1×10^{13} W/cm^2, (b) 5×10^{13} W/cm^2, 2×10^{14} W/cm^2 and (b) 5×10^{14} W/cm^2

At lower intensities, signatures of the adiabatic as well as non-adiabatic behavior are present with adiabatic features are most dominant. However, as the intensity is increased the Rabi oscillations due to the orbital coupling get stronger and compete with the adiabatic oscillation of the electron. At the highest intensities, strong non-adiabatic behavior is visible. Thus, the electron dynamics within the molecule is governed by both adiabatic and non-adiabatic

response to the laser field when there is a coupling between two orbitals. By tuning the intensity of the field, and controlling the Rabi oscillations, it is possible to control the non-adiabatic effects.

3.4 Non-adiabatic Electron Localization in Two-Color Laser Fields

So far the results presented have been driven by a single laser pulse. It is also interesting to see if the competing processes can be controlled by superposing two fields. To this end we considered a resonant 400 nm field of intensity $\mathrm{I} = 5 \times 10^{12}\ W/cm^2$, and a second 800 nm field of intensity $\mathrm{I} = 5 \times 10^{13}\ W/cm^2$. Simulations of N_2^+ interacting with this two-color field were performed, with one case having both laser field polarizations parallel to the molecular axis and the other case having the 800 nm component perpendicular and the 400 nm component parallel to the molecular axis. The results of the simulations are shown in Figure 3.4.
In Figure 3.4(a) the resonant component is the 400 nm field, thus Rabi oscillations should show up, though at a relatively low frequency due to the lower intensity of the field. It is therefore expected that the adiabatic behavior driven by the 800 nm field is overlapped by non-adiabatic behavior at a lower frequency. This is indeed what we see in Figure 3.4(a). Figure 3.4(b) presents the case where the 800 nm field is oriented perpendicular to the molecular axis therefore it induces another coupling between the HOMO and HOMO-1, as previously discussed. This results in a competition between the induced coupling by the 400 nm field and that by the 800 nm field. Thus, overall we observe a much stronger and qualitatively different non-adiabatic behavior than in the first case considered.

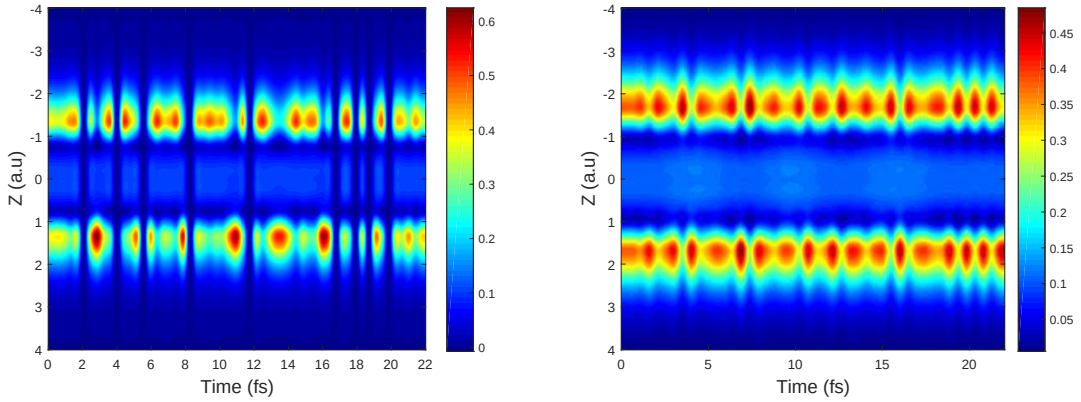

(a) (b)

Figure 3.4: Visualization of non-adiabatic behavior within the electron localization of N_2^+ under the influence of a two-color laser field in which (a) the resonant 400 nm and the non resonant 800 nm components are oriented parallel to the molecular axis, and (b) where the 800 nm component is perpendicular and the 400 nm component parallel to the molecular axis and both induce couplings between orbitals.

3.5 Summary

In this chapter, non-adiabatic behavior of electron dynamics was investigated in context to electron localization in N_2^+. This non-adiabatic behavior is a consequence of two competing processes: Electron following the oscillations of the electric field, and the Rabi oscillations brought upon by induced coupling of orbitals. It was shown that the competing processes are strongly dependent on the intensity of the laser field, and by varying the intensity it is possible to control the non-adiabatic effects present in the dynamics. In addition, simulations were conducted with a two-color field to investigate the possibility of controlling the adiabatic and non-adiabatic behavior.

Chapter 4

Multielectron Effects in High Harmonic Generation

The study of HHG has been focused on atoms for almost three decades now resulting in thorough understanding of the basic properties. However HHG has been observed from molecules as well. The semi-classical three-step model for HHG can give a deeper understanding of the contributions from molecules. In step 1 of the model, the bound electron is ionized by the applied field; in molecules the rate of ionization is dependent on the molecular symmetry. Step 2 involves the acceleration of the electron by the field, and step 3 the recombination of the electron with the parent ion. Within these steps there is a possibility of constructive and destructive interference of the electron wavepacket for example due to the recombination of the electron wavepacket at different nuclei in the molecule. If the quantum interference in the last two steps does not cancel out the effect of the first step, then ionization may be enhanced and the HHG yield will be increased [17].

Besides this phenomenon, effects due to multielectron nature of the molecule may arise. In this chapter, several multielectron effects are discussed in relation to HHG, in particular the presence of fractional harmonics. Fractional harmonics arise in addition to the odd harmonics when the optical frequency of the laser field is the same as the frequency of transition between an inner valence orbital and an electron hole in the highest occupied molecular orbital (HOMO) of the molecule.

4.1 Fractional Harmonics

4.1.1 Adiabatic and Non-adiabatic Behavior of Laser Induced Dipole

HHG spectra for a system can be obtained by taking a Fourier Transform of the laser induced dipole. Within the context of TDDFT, the dipole is given by

$$\mathbf{d}_{total} = \sum_i \mathbf{d}_i, \tag{4.1}$$

where $\mathbf{d}_i$ is the dipole corresponding to the i^{th} orbital, which is given by

$$\mathbf{d}_i = \langle \phi_i(\mathbf{r},t)|\mathbf{r}|\phi_i(\mathbf{r},t)\rangle = \int \phi_i(\mathbf{r},t)^* \mathbf{r} \phi_i(\mathbf{r},t) d\mathbf{r}. \tag{4.2}$$

In N_2^+ there is an energy difference between the HOMO and HOMO-2 that corresponds to a wavelength of 400 nm. Figure 4.1 below presents the results of two simulations in the case of an applied trapezoidal envelope laser pulse of the same wavelength, an intensity of $2\text{x}10^{14}\text{W/cm}^2$, and a pulse length 16 fs.

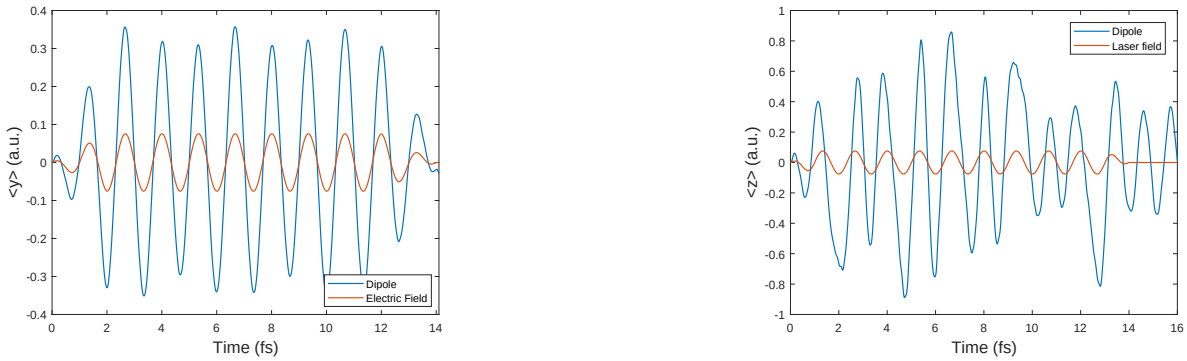

(a) (b)

Figure 4.1: Laser induced dipole for cases when a 400 nm laser field of 2×10^{14} W/cm^2 is applied with polarization direction (a) perpendicular and (b) parallel to the molecular axis.

In case (a) the laser field is applied perpendicular to the molecular axis and the dipole exhibits

adiabatic behavior (i.e. dipole follows the electric field). In case (b), where the polarization of the field is parallel to the molecular axis, there is an induced coupling between the HOMO and HOMO-2, therefore the dipole behavior is non-adiabatic, i.e. the dipole does not follow the electric field.

4.1.2 Fractional Harmonics in HHG

Due to the laser induced resonant coupling between orbitals and the non-adiabatic behavior of the dipole, some additional features appear in the HHG spectrum. This can be seen for N_2^+ interacting with a 400 nm laser pulse, where there is an orbital coupling between HOMO and HOMO-2 when the molecular axis is oriented parallel to the laser polarization; but also at 800 nm, when the orbital coupling between HOMO and HOMO-1 occurs for perpendicular orientation. Figure 4.2 shows a comparison of the HHG spectra for the two cases where N_2^+ interacts either with a pulse at 400 nm or 800 nm and orientations in which orbital coupling is observed and not observed.

The sidebands, which appear next to odd harmonics in the case of orbital coupling, are referred to as fractional harmonics, as they do not appear at integer multiples of the optical frequency, but rather as fractions of the optical frequency. These fractional harmonics are a consequence of the laser induced coupling of orbitals. The fractional harmonics are quite intense relative to the odd harmonics; which is due to the large transition dipole matrix element between the orbitals [1,8].

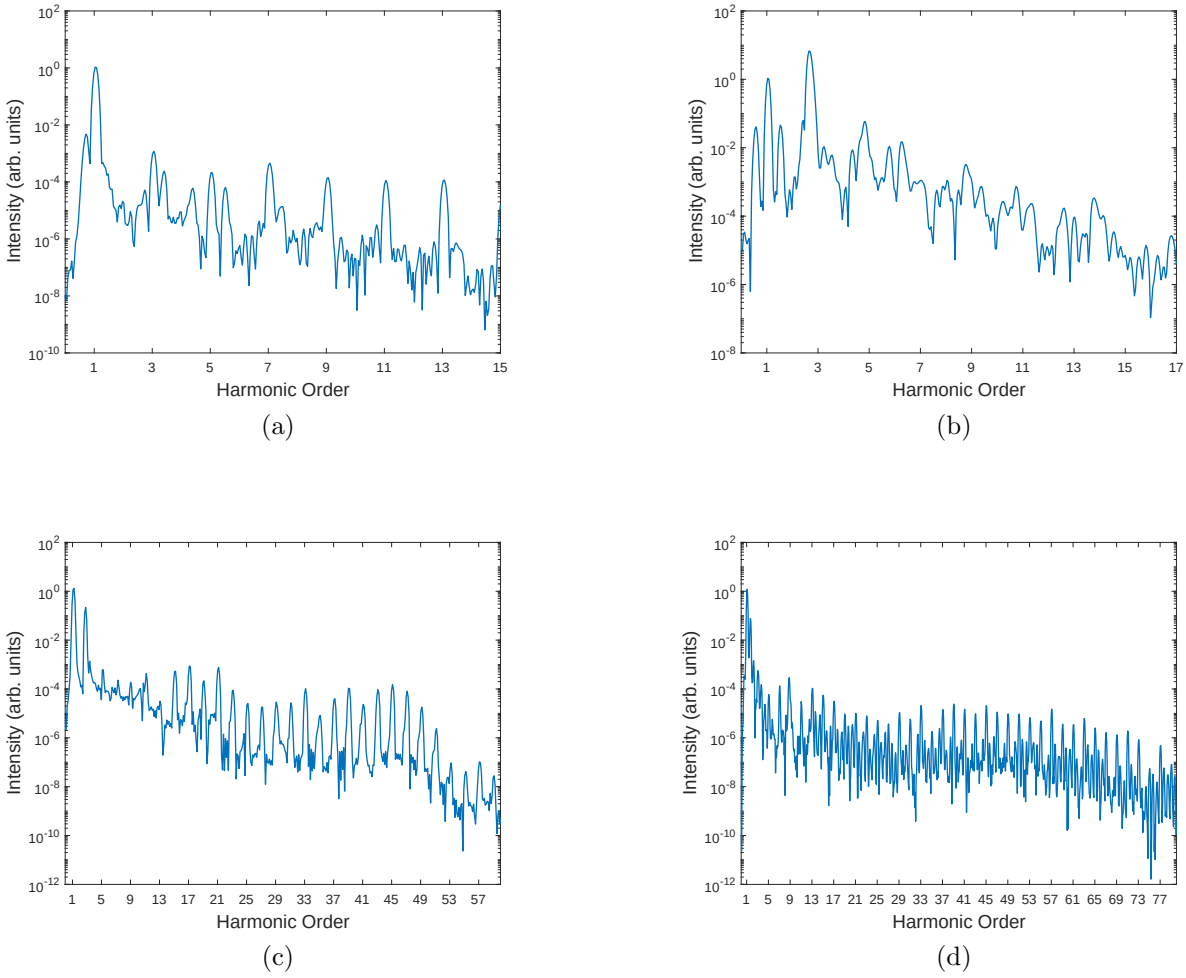

Figure 4.2: HHG spectra of N_2^+ (a) aligned perpendicular, and (b) aligned parallel to a 400 nm laser pulse of intensity I $= 2 \times 10^{14}$ W/cm^2, as well as (c) aligned parallel and (d) aligned perpendicular to an 800 nm laser of intensity I $= 2 \times 10^{14}$ W/cm^2 .

The mechanism responsible for the appearance of the fractional sidebands is analogous to the Autler-Townes effect, which can be described with the help of the so-called dressed states. Consider a two-level system with eigenstates $|g\rangle$ and $|e\rangle$. When a resonant laser field is applied, the two eigenstates are no longer eigenstates of the new Hamiltonian which includes the interaction with the laser field. Instead, the two original eigenstates are split into doublets or "dressed states". Thus, laser induced interaction creates two states $|+, n\rangle$ and $|-, n\rangle$, separated by a detuning Δ. The index n denotes the photon number in the laser field mode. The two states are separated by an energy corresponding to the Rabi frequency Ω_R. Figure

4.3 shows the allowed transitions between the dressed states.

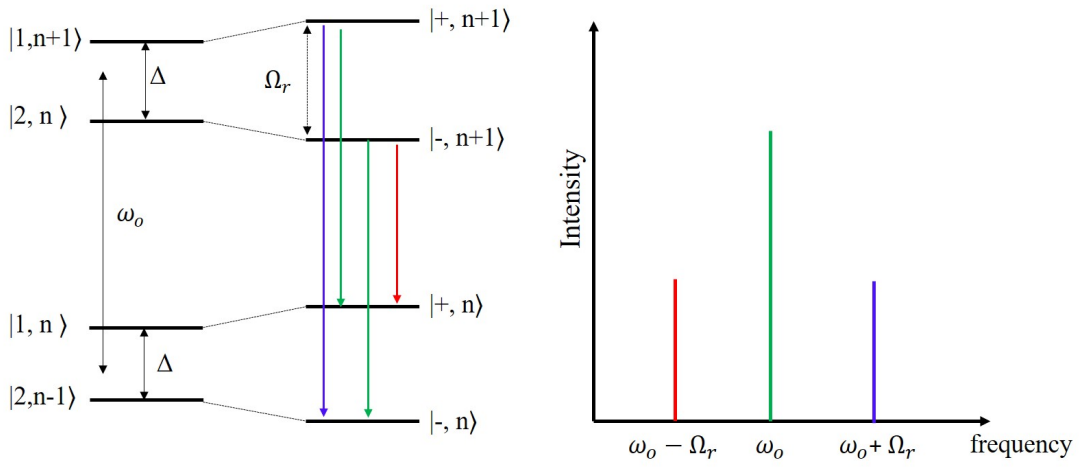

Figure 4.3: Illustration of the allowed transitions between dressed states (left) and schematic representation of Mollow triplets in fluorescence spectrum (right).

As shown, there are three possible emission frequencies ω_o, $\omega_o - \Omega_r$, and $\omega_o + \Omega_r$, where Ω_r is the Rabi frequency, given by

$$\Omega_r = \frac{\mu E}{\hbar}, \tag{4.3}$$

where μ is the transition dipole matrix element, and E is the electric field. The structure with sidebands appearing in the fluorescence spectrum is referred to as Mollow triplets. In the following section, the fractional harmonics are studied for a varying laser intensity, to determine the relationship between the fractional harmonics and the Rabi frequency.

4.2 HHG Dependence on Laser Intensity

The non-adiabatic behavior is observed for interactions at high laser intensities. It is therefore interesting to analyze how HHG spectra change when laser intensity is increased. Several simulations of N_2^+ interacting with a 400 nm laser pulse were performed for the following laser intensities: 1×10^{13} W/cm^2, 5×10^{13} W/cm^2, 2×10^{14} W/cm^2, and 5×10^{14} W/cm^2. In Figure 4.4 we present the HHG spectra for these cases.

For the different intensities HHG spectra appear to vary widely. At the lower intensities of $1 \times 10^{13}\ W/cm^2$ and $5 \times 10^{13}\ W/cm^2$ there are fractional harmonics produced, but their respective peaks appear to be overlapping greatly with the odd harmonics. Due to the overlap it cannot be easily determined how many sidebands of fractional harmonics are indeed generated. At higher intensities of $2 \times 10^{14}\ W/cm^2$ and $5 \times 10^{14}\ W/cm^2$ the resolution between peaks is much better and the fractional harmonics can be distinguished from the odd harmonics. It also appears that as the intensity is increased more fractional harmonics, i.e. higher order of the sidebands, appear next to the odd harmonics in the spectrum.

The features can be qualitatively described as follows: when the molecule interacts with a laser field that induces orbital coupling, there is a competition between the oscillation at the Rabi frequency and the oscillation with the frequency of the electric field. At the lower intensities the dominating process is high harmonic generation driven by the field. However, as the intensity is increased the strength of the Rabi oscillations increases rapidly and competes more and more with the oscillations of the electric field. Therefore we can expect that more and stronger fractional harmonics appear as the laser field intensity is increased.

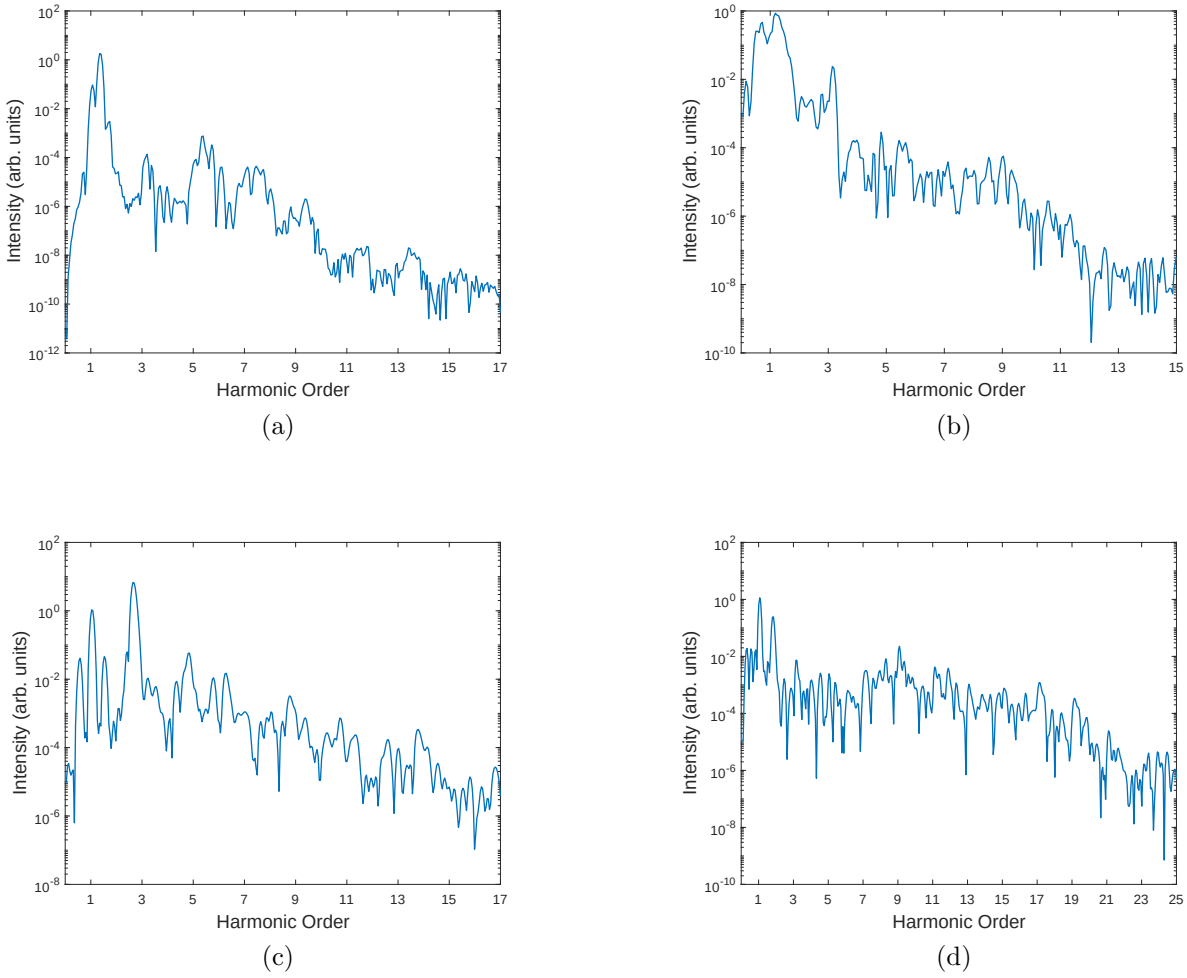

Figure 4.4: HHG spectra of N_2^+ (a) aligned perpendicular and (b) aligned parallel to a 400 nm laser pulse of intensity I $= 2 \times 10^{14}$ W/cm^2, as well as (c) parallel and (d) perpendicular to a 800 nm laser of intensity I $= 2 \times 10^{14}$ W/cm^2.

4.3 High Harmonic Generation in Two-Color Laser Field

So far, the two competing processes observed in the laser induced coupling have been driven by a single laser pulse. However, it is interesting to consider a two-color experiment in which each process is controlled separately by two laser pulses. In this section, the results of simulations with two-color laser pulses are presented. The fields considered are a 400 nm resonant field at intensity I $= 5 \times 10^{12}$ W/cm^2 used to control the coupling between orbitals, and a second 800 nm non-resonant field at intensity I $= 5 \times 10^{13}$ W/cm^2, which is responsible

for inducing HHG. While it is clear that both processes cannot be separated completely due to the resonant field contributing to both processes, it is still interesting to study how the effects can be controlled with both fields.

N_2^+ is once again studied with one case having both fields parallel to the molecular axis, and in the other the 400 nm field is parallel while the 800 nm field is perpendicular to the molecular axis. Figure 4.5 presents the respective HHG spectra produced from both simulations.

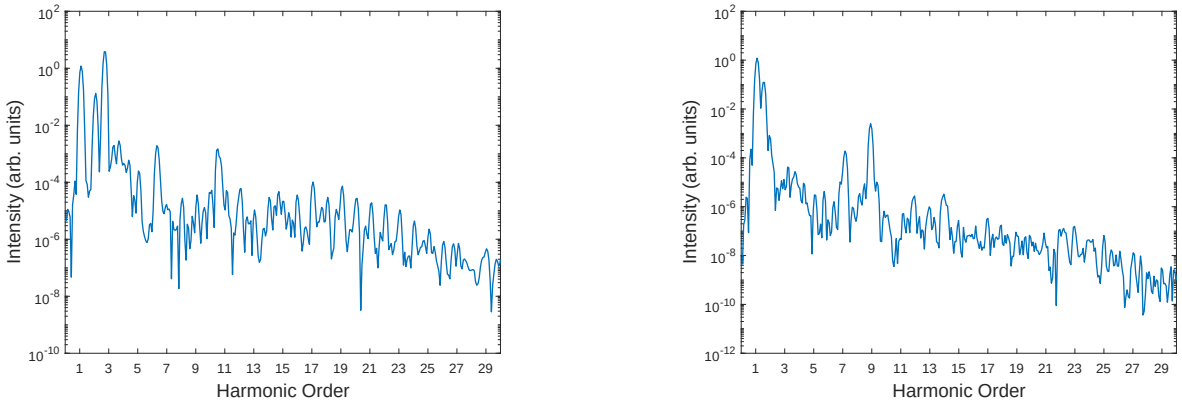

(a) (b)

Figure 4.5: The HHG spectra of N_2^+ where (a) both fields are aligned parallel to the molecular axis, and where (b) the resonant field is aligned parallel, and the non-resonant field is aligned perpendicular to the molecular axis.

When both fields are aligned parallel to the molecular axis, there will be an induced resonant coupling between HOMO and HOMO-2 due to the 400 nm laser. Therefore, fractional harmonics are observed in the HHG spectrum. The nonresonant 800 nm laser pulse of higher intensity is driving the nonlinear dynamics that leads to HHG and appearance of odd harmonics. When the polarization direction of the 800 nm laser pulse is perpendicular to the molecular axis there is an induced coupling between the HOMO and HOMO-1 at that wavelength. Overlap between the odd harmonics and the fractional harmonics produced is evident in the HHG spectrum, which in turn provides no clear resolution as to how many

fractional harmonics are produced. This overlap could be due to the competing processes of the 400 nm induced coupling and the 800 nm induced coupling, as both components of the two-color field are resonant.

4.4 Summary

In this chapter, the appearance of fractional harmonics in high harmonic spectra is presented. These fractional harmonics are a consequence of the laser induced coupling (Rabi flopping) between an inner valence orbital and the outer orbital. The appearance of the fractional harmonics is presented for parallel (σ-σ) transitions and perpendicular (σ-π) transitions in N_2^+. The relation between fractional harmonics and varying laser intensity is also presented, and confirms that the appearance of the fractional harmonics is due to the non-adiabatic behavior of the electron density in the molecule.

Chapter 5

Multielectron Effects in Strong-Field Ionization in N_2^+

Ionization is one of the fundamental AMO processes but can also be considered as a tool from which information about the dynamics of the system can be extracted. In particular recent advances in attosecond science allow for application of pump-probe experimental techniques such as streaking [18] to study the ionization of electrons at the ultrafast scale and give insight into electron dynamics occurring within systems. The description of ionization in molecules is more complicated than the quasi-static picture in atoms, such as tunneling ionization.

In this chapter, we study if the coupling between two orbitals, that previously has been shown to lead to non-adiabatic behavior of the electron dynamics and the occurrence of fractional harmonics, leads to changes in ionization of molecules by strong laser pulses.

5.1 Resonance Enhanced Ionization of N_2^+

Within TDDFT, the Kohn-Sham orbitals are propagated in time under the influence of an external laser field. The population $n(t)$ of the i^{th} orbital at a given time t can be obtained by integrating the square modulus of the corresponding orbital wavefunction, as given by

$$n_i^{ks}(t) = \int f_i |\phi_i(\mathbf{r}, t)|^2 d\mathbf{r}, \tag{5.1}$$

where the i^{th} Kohm-Sham orbital is denoted by $\phi_i(\mathbf{r}, t)$, and f_i the occupation number of

that orbital. The ionization of the i^{th} orbital is then given by

$$P_i(t) = 1 - n_i^{ks}(t). \tag{5.2}$$

As previously discussed, there is a laser induced resonant coupling in N_2^+ for HOMO and HOMO-2 with a 400 nm field (for parallel orientation) and HOMO and HOMO-1 with an 800 nm field (for perpendicular orientation). For both cases, our numerical results show that the induced laser coupling can enhance the ionization from the HOMO-2 and HOMO-1. In our simulation, the system was prepared in such a way that the hole present in the HOMO corresponds to a spin down electron. Figure 5.1 shows the ionization probabilities for spin up and down electrons in N_2^+ interacting with a 400 nm and 800 nm field of intensity I = 2×10^{14} W/cm^2.

It is expected that the HOMO would have the largest probability of ionization due to its smaller ionization potential. However, this is not always observed. When there is an electron hole present in the HOMO, and there is an induced coupling between states, there is a resonant enhanced ionization of the inner shell electron. In the case of resonant coupling at 400 nm, the HOMO-2 contributes most to total ionization yield, the HOMO-1 contributes the most when there is a resonant coupling at 800 nm.

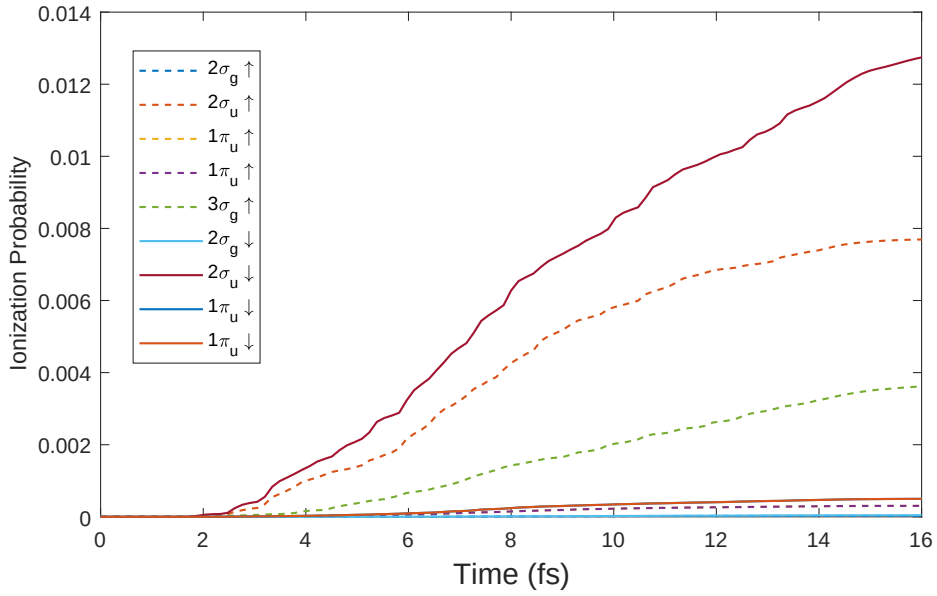

(a)

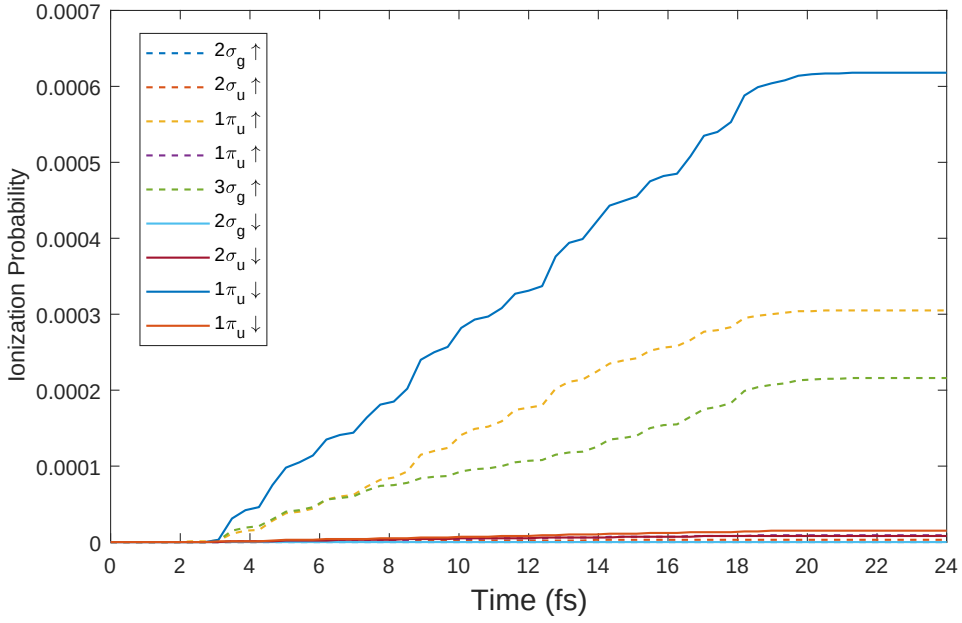

(b)

Figure 5.1: Ionization yields of N_2^+ in the regime of orbital coupling induced by (a) a 400 nm field, and (b) a 800 nm field. The results include the ionization for both spin up and down electrons. The laser intensity is I $= 2 \times 10^{14}$ W/cm^2 for each case.

Because the electron hole is in the spin down orbital of the HOMO, the ionization yield

should be greater from the spin down electron in the HOMO-1 for 800 nm induced coupling and HOMO-2 for 400 nm induced coupling. This is indeed what the results obtained from our simulations show.

5.2 Summary

In this chapter, ionization of N_2^+ was analyzed in the regime where orbital coupling is observed. It would be expected that the HOMO would contribute the most to the total ionization yield. However, due to resonant enhanced ionization brought upon by laser induced coupling of states, the major contribution to ionization may be from the inner shell orbitals, HOMO-2 (when the laser field is at 400 nm), and HOMO-1 (when the laser field is at 800 nm).

Chapter 6

Summary and Discussion

In this thesis, time dependent density-functional theory was used to study multielectron effects in high-harmonic generation, ionization and electron localization during the interaction between molecules and high intensity lasers. In particular, it was shown that laser induced coupling of states leads to some very interesting phenomena, which are visualized within the results.

In chapter 3, non-adiabatic behavior is studied in the context of electron localization. It was determined that the two competing processes, namely oscillation of the electron dynamics with the electric field, and Rabi flopping induced by orbital coupling, lead to strong non-adiabatic behavior in electron localization. Furthermore, it was determined that there is a strong relation between laser intensity and non-adiabatic behavior. In addition, two-color simulations were performed to show how both processes could be controlled by using simultaneously two laser pulses.

In chapter 4, multielectron effects in high-harmonic generation were analyzed, and it was determined that laser induced coupling of states leads to the appearance of fractional harmonics in the form of Mollow sidebands in the respective HHG spectra. It was also determined that there is a strong relationship between the intensity of the laser and the appearance of the fractional harmonics, which come as a result of non-adiabatic behavior.

In chapter 5, ionization of N_2^+ was studied. The results presented show that laser induced coupling of states enhances the contribution from inner shell orbitals to ionization. From

this, it can be concluded that multielectron effects within the strong field regime contribute vastly to the electron dynamics.

Bibliography

[1] Y. Xia, and A. Jaron-Becker. *Mollow sidebands in high order harmonic spectra of molecules*. Opt. Exp., **24**:4689, (2016).

[2] T. Popmintchev, M. C. Chen, P. Arpin, M. M. Murnane, and H. C. Kapteyn. *The attosecond nonlinear optics of bright coherent X-ray generation.*. Nat. Photonics, **4**:822832, 2010.

[3] A. Castro, H. Appel, Micael Oliveira, C.A. Rozzi, X. Andrade, F. Lorenzen, M.A.L. Marques, E.K.U. Gross, and A. Rubio. *Octopus: a tool for the application of time-dependent density functional theory*. Phys. Stat. Sol. B **243**: 2465-2488 (2006).

[4] X. Andrade, D. A. Strubbe, U. De Giovannini, A. H. Larsen, M. J. T. Oliveira, J. Alberdi-Rodriguez, A. Varas, I. Theophilou, N. Helbig, M. Verstraete, L. Stella, F. Nogueira, A. Aspuru-Guzik, A. Castro, M. A. L. Marques, and A. Rubio. *Real-space grids and the Octopus code as tools for the development of new simulation approaches for electronic systems*. Phys Chem Chem Phys **17**: 31371-31396 (2015).

[5] M.A.L. Marques, A. Castro, G. F. Bertsch, and A. Rubio. *Octopus: a first-principles tool for excited electron-ion dynamics*. Comput. Phys. Commun. **151**: 60-78 (2003).

[6] A.L. Marques, N.T. Maitra, F. Nogueira, E.K.U. Gross, and A. Rubio (Eds.), Lecture Notes in Physics, Vol. 837. *Fundamentals of time-dependent density functional theory*. (Springer, Berlin), (2012), ISBN: 978-3-642-23518-4.

[7] M.A.L. Marques and E.K.U. Gross. *Time-dependent density functional theory*. Annu. Rev. Phys. Chem. **55**: 427-455 (2004).

[8] M.R Miller, Y. Xia, A. Becker and A. Jaron-Becker. *Laser driven nonadiabatic electron dynamics in molecules*. Optica **3**: 259-269 (2016)

[9] A. Castro, M.A Marques, and A. Rubio. *Propagators for the time-dependent KohnSham equations*. J. Chem. Phys. **121**: 3425 (2004).

[10] Sang-Kil Son, D. A. Telnov, Shih-I Chu. *Probing the origin of elliptical high-order harmonic generation from aligned molecules in linearly polarized laser fields*. Phys. Rev. A. **82**, 043829 (2010).

[11] J. Anderson, P. J. Burns, D. Milroy, P. Ruprecht, T. Hauser, and H. J. Siegel. *Deploying RMACC Summit: An HPC Resource for the Rocky Mountain Region.*. In Proceedings of PEARC17, New Orleans, LA, USA, July 09-13, 2017. DOI: 10.1145/3093338.3093379

[12] E. Muybridge *The horse in motion*. URL http://hdl.loc.gov/ loc.pnp/cph.3a45870.

[13] M. A. L. Marques, M. J. T. Oliveira, and T. Burnus. *Libxc: a library of exchange and correlation functionals for density functional theory*. Comput. Phys. Commun., **183**, 2272-2281 (2012).

[14] C. Legrang, E. Suraud, and P.-G. Reinhard. *Comparison of self-interaction-corrections for metal clusters*. J. Phys. B: At. Mol. Opt. Phys. **35** 1115 (2002).

[15] D.M. Gaudiosi, B.A. Reagan, T. Popmintchev, M.E. Grisham, M.A. Berrill, O. Cohen, B.C. Walker, M.M Murnane, H.C. Kapteyn, J.J. Rocca. *High harmonic generation from ions in a capillary discharge plasma waveguide*. Optics and Photonics News Vol. 17, Issue 12, 44 (2006).

[16] D. Popmintchev, C. Hernandez-Garca, F. Dollar, C. Mancuso, J. Perez-Hernandez, M.C. Chen, A. Hankla, X. Gao, B. Shim, A. Gaeta, M. Tarazkar, D. Romanov, R. Levis, J. Gaffney, M. Foord, S. Libby, A. Jaron-Becker, A. Becker, L. Plaja, M. Murnane, H. Kapteyn, and T. Popmintchev. *Efficient soft X-ray high harmonic generation in multiply-ionized plasmas: the ultraviolet surprise*. Science, **350**: 1225, (2015).

[17] T. Zuo and A. D. Bandrauk. *Charge-resonance-enhanced ionization of diatomic molecular ions by intense lasers*. Phys. Rev. A **52**, R2511(R) (1995).

[18] M. Kbel, Z. Dube, A.Yu. Naumov, M. Spanner, G.G. Paulus, M.F. Kling, D.M. Villeneuve, P.B. Corkum, and A. Staudte. *Streak Camera for Strong-Field Ionization*. Phys. Rev. Lett. **119**, 183201 (2017).